Geophysical Research Letters

RESEARCH LETTER
10.1029/2022GL100561

Key Points:

- Hazard assessments in monogenetic volcanic fields have considered pyroclastic surge runout up to 6 km based upon preserved deposits of previous eruptions
- Surge deposits from Ubehebe Crater extend to 9 km; this may not be unusual and such surges may have long runout facilitated by their low temperatures
- We suggest that future hazard assessments in monogenetic volcanic fields consider pyroclastic surge runout up to 10–15 km

Correspondence to:
G. A. Valentine,
gav4@buffalo.edu

Citation:
Valentine, G. A., Fierstein, J., & White, J. D. L. (2022). Lateral extent of pyroclastic surge deposits at Ubehebe Crater (Death Valley, California) and implications for hazards in monogenetic volcanic fields. *Geophysical Research Letters*, *49*, e2022GL100561. https://doi.org/10.1029/2022GL100561

Received 27 JUL 2022
Accepted 27 SEP 2022

Author Contributions:
Conceptualization: Greg A. Valentine, Judy Fierstein, James D. L. White
Funding acquisition: Greg A. Valentine, Judy Fierstein, James D. L. White
Investigation: Judy Fierstein, James D. L. White
Methodology: Greg A. Valentine
Software: Greg A. Valentine
Visualization: Greg A. Valentine
Writing – original draft: Greg A. Valentine
Writing – review & editing: Judy Fierstein, James D. L. White

Lateral Extent of Pyroclastic Surge Deposits at Ubehebe Crater (Death Valley, California) and Implications for Hazards in Monogenetic Volcanic Fields

Greg A. Valentine[1], Judy Fierstein[2], and James D. L. White[3]

[1]Department of Geology, University at Buffalo, Buffalo, NY, USA, [2]U.S. Geological Survey, Volcano Science Center, Menlo Park, CA, USA, [3]Department of Geology, University of Otago, Dunedin, New Zealand

Abstract Hazard assessments in monogenetic volcanic fields require estimates of the runout of pyroclastic surges that result from phreatomagmatic explosive activity. Previous assessments used runout distances of 1–4 km, with large cases up to 6 km. Surge deposits at Ubehebe Crater (~2100 y.b.p., Death Valley, California) have been traced ~9 km from the crater center, and likely originally extended 1–3 km farther. There is no evidence that the Ubehebe Crater activity was unusually energetic; rather, its distal deposits are better preserved than those at most maar volcanoes because of its young age and the arid environment. Numerical simulations illustrate how low temperatures facilitate long runout of phreatomagmatic surges due to reduced expansion of entrained air compared to hot surges, allowing cool surges to retain higher densities than ambient air. We suggest that hazard assessments for volcanic fields with phreatomagmatic, maar-forming eruptions should consider runout distances in the range of 10–15 km.

Plain Language Summary Assessments of volcanic hazards in areas prone to small-volume basaltic volcanoes includes consideration of the lateral extent of devastating pyroclastic surges from eruptions that are caused by magma-water explosions. Previous assessments considered surge distances up to 6 km, but the deposits from Ubehebe Crater (Death Valley, California, USA) have been traced to 9 km and likely originally extended farther. This was not an unusual eruption, but its deposits are exceptionally preserved due to the arid environment. Pyroclastic surges from magma-water explosions are likely to be cooler than other volcanic flows, and this facilitates long travel distances and hence far-reaching potential impacts if the area is inhabited. We suggest that future assessments should consider pyroclastic surge distances of 10–15 km from the vent.

1. Introduction

Basaltic volcanic fields may contain hundreds of small, monogenetic volcanoes, and some portion of these are maar volcanoes produced by explosive interaction of magma and groundwater (phreatomagmatic; Valentine & Connor, 2015; White & Ross, 2011). A major hazard during maar-forming eruptions is from ground-hugging, dilute pyroclastic currents (here referred to as pyroclastic surges). Hazard assessments and emergency planning in volcanic fields requires estimates of pyroclastic surge runout distances. Previous hazard assessments and emergency planning studies used runout distances that are based largely on extents of previous deposits in the geologic record (e.g., Sandri et al., 2012; Wild et al., 2021), but thin, unconsolidated deposits that would record distal pyroclastic surges are notoriously poorly preserved due to erosion, bioturbation, and weathering. This calls into question whether such runout distances are really representative, or to what degree they may result in underestimated hazards.

Here we document the lateral extent of pyroclastic surge deposits associated with Ubehebe Crater, a maar in Death Valley (California, USA). These deposits are observed to a distance of 9 km from their source vent. Ubehebe Crater's distal deposits are preserved due to their young age and the extremely dry and vegetation-poor environment; there is no reason to believe that these were produced by unusual explosive events. We illustrate how low surge temperatures expected from phreatomagmatic explosions can enhance runout compared to hotter pyroclastic surges. Low temperatures are considered to be typical of maar-related surges.

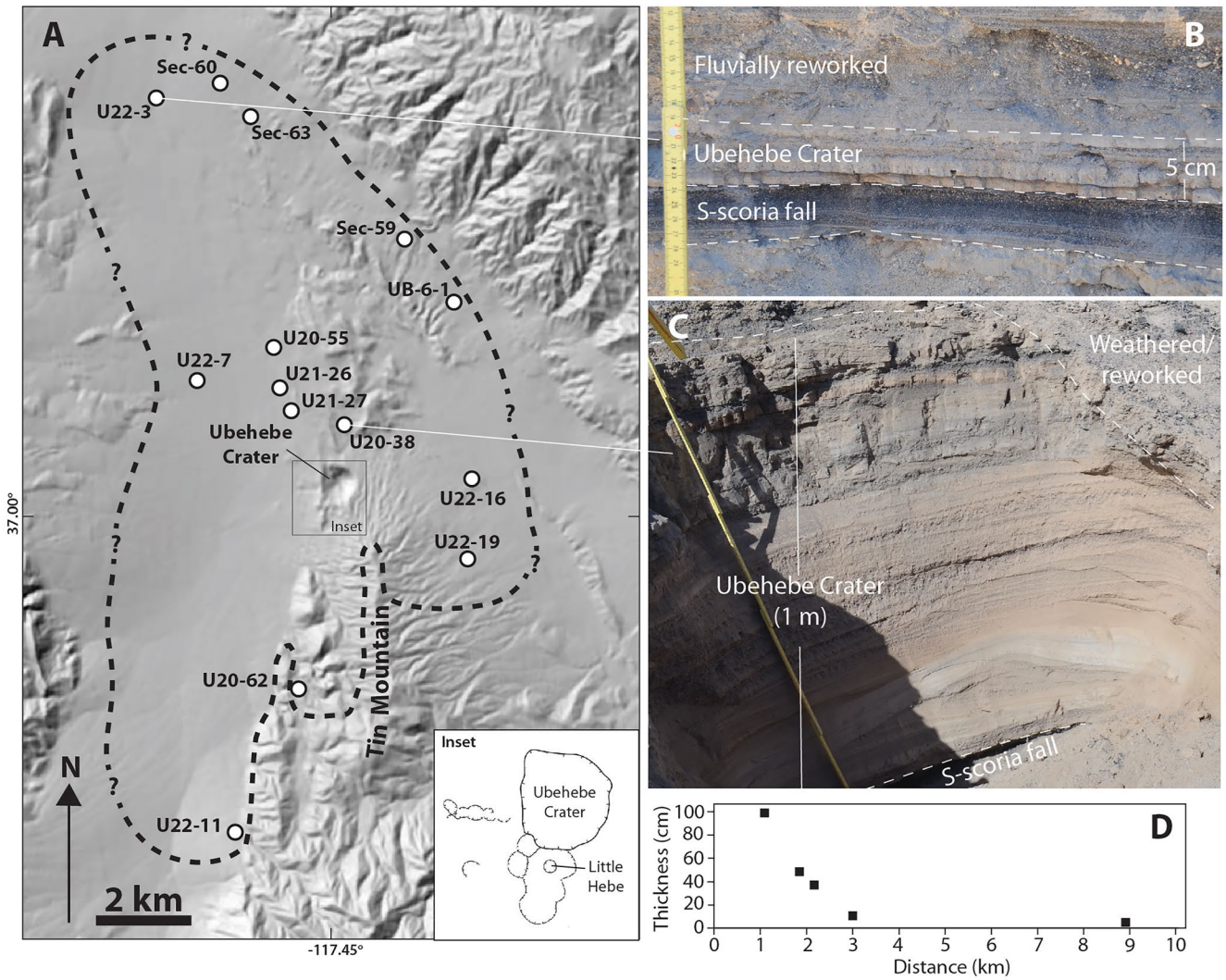

Figure 1. (a) Shaded relief map showing Ubehebe Crater and the lateral extent of its pyroclastic surge deposits and the study sites that define that extent or are otherwise referred to in this paper (Table 1). Question marks are areas of high uncertainty due to active alluvial fans. Shaded relief from https://apps.nationalmap.gov/3depdem/. Inset shows outlines of preserved craters at the volcanic center (Fierstein & Hildreth, 2017). (b) Photograph of northernmost Ubehebe Crater deposits, 9 km from crater center (station U22-3) and totaling 5 cm in thickness. These deposits are underlain by S-scoria from the opening phase of the Ubehebe volcanic center, and overlain by fluvially reworked material. Ubehebe Crater deposits here are planar-parallel laminated ash with similar tan to light gray color variations to those observed in other locations north of the crater, and are capped by a 1 cm-thick, very fine ash layer that likely records settling of fines after surges were emplaced. (c) Photo of medial Ubehebe Crater deposits, 1.1 km north of the crater center, for comparison. Here the deposits total 1 m thick and consist of numerous laminated and cross-laminated, fine-to coarse-ash horizons and some layers include small lapilli. (d) Thickness of laminated and cross-laminated (pyroclastic surge) deposits as a function of distance along a north-northwest transect with minimal topographic variation (number of points limited due to sparse preservation along distal portions of the transect). Sites plotted, in order of increasing distance from crater center, are: U20–38, U21–27, U21–26, U20–55, and U22-3 (Table 1).

2. Ubehebe Crater

Ubehebe Crater was produced during the final activity of the monogenetic Ubehebe volcanic center (~2,100 y.b.p.; Champion et al., 2018). Fierstein and Hildreth (2017) described how the center's eruptive episode began with development of an initial scoria cone and associated widespread fall deposit, then transitioned to phreatomagmatic activity, which formed several explosion craters surrounded by locally distributed, lithic-rich ejecta (Figure 1a). Late in the eruptive episode a small cone of variably welded agglomerate (Little Hebe) with a localized fall deposit formed, followed by two more phreatomagmatic explosion craters. Explosions and collapse during the last of these, which produced Ubehebe Crater (the largest of the craters), obliterated much of the initial scoria cone, leaving only a remnant exposed in the crater walls. Stratigraphic relations between the products of all the craters are detailed in Fierstein and Hildreth (2017). Ubehebe Crater has a diameter of ~800 m and is ~150 m

deep (measured from rim to rim and from rim to crater floor), cutting into the pre-eruptive landscape and exposing the underlying Miocene fanglomerate country rock in its walls. Magma responsible for all of the explosive activity was trachybasaltic (Crowe & Fisher, 1973), here loosely referred to as basalt.

Ubehebe Crater deposits fall into three main facies types with their inferred emplacement mechanisms (Valentine et al., 2022). One type is related to ballistic processes and is found within ~700–1,000 m from the crater center. The most widespread facies type, and the focus of this paper, is dominated by laminated and cross-laminated ash out to the most distal deposits, with a component of coarser-grained, thinly bedded lapilli tuffs in proximal areas within several hundred meters of the crater center; these are interpreted to have been produced by pyroclastic surges. A third facies type includes massive lapilli ash/tuff beds found in channel bottoms; this facies is interpreted to record concentrated, dry granular flows that originated through rapid deposition and slumping of surge deposits on steep slopes above the channels. Although not further discussed here, these surge-derived, concentrated flows followed paths of their own down drainages and onto valley floors below. They represent a previously unconsidered hazard at maar volcanoes.

We estimate the total volume of Ubehebe Crater deposits to be $\sim 3 \times 10^7$–5×10^7 m^3. This estimate is based on the volume of the excavated crater, measured from the contact between ejecta and country rock exposed in the crater walls, and allowing for an additional, poorly constrained, volume of recycled basalt clasts from the small initial scoria cone that was largely co-located with the crater, plus primary juvenile fragments that were directly involved in the phreatomagmatic explosions that excavated the crater (White & Houghton, 2006). Limited component analysis indicates that ~50–90 vol.% of ash in the deposits is some combination of recycled and primary juvenile basalt with the remainder being country rock fragments. Primary juvenile ash can be difficult to distinguish from recycled basaltic grains; this is a subject of ongoing study. Primary juvenile bombs are rare in the Ubehebe Crater deposits while primary juvenile lapilli-size clasts are common in some individual layers. Another approach to calculating deposit volume would be to use the deposit itself; however, much of it was dispersed over very rugged terrain where it may have been later stripped, and it has quite variable thickness where preserved. We view our volume estimates as reasonable, given the crater-excavating nature of subsurface phreatomagmatic explosions (e.g., Valentine & White, 2012; White & Ross, 2011).

3. Lateral Extent of the Ubehebe Crater Pyroclastic Surge Deposits

Ubehebe Crater deposits have been documented in detail at 79 sites throughout their extent and numerous others in less detail, but here we highlight sites that reveal the most distal preserved deposits (Figure 1a; Table 1). These deposits are up to ~9 km to the north, and ~7 km to the south-southeast, of the crater center. Areas lacking observed Ubehebe Crater deposits, such as west-southwest and directly east of the crater, are active alluvial fans, where thin ash layers would have been eroded or buried in the ~2100 years since emplacement. High terrain directly south of the crater appears to have reduced surge runout in that direction. Stratified scoria fall, related to the initial scoria cone-building phase of the eruptive sequence (Fierstein & Hildreth, 2017), underlies the Ubehebe Crater deposits at most locations.

Ubehebe Crater products are preserved in isolated patches at distal locations north and northwest of the crater, where topography is relatively subdued. In these areas the deposits are planar-laminated, fine to medium ash (Figure 1b), similar to distal deposits observed at other maars (e.g., Vazquez & Ort, 2006). The distal deposits are lateral equivalents of coarser and thicker, planar-to cross-laminated, fine to coarse ash strata that are found within ~2 km from the crater center (Figure 1c). Thicknesses of laminated to cross-laminated ash deposits decay exponentially with distance along a relatively low-relief, approximately radial path leading north-northwest from the crater (Figure 1d). Such thinning is a combined result of sedimentation from the turbulent currents (e.g., Bursik et al., 1998) and of multiple surges that reached different distances, with shorter runout events being more common than those with long runout.

At sites U20–62, U22–11, U22-16, and U22-19 (Figure 1a), Ubehebe Crater deposits are massive lapilli ash/tuff, locally with diffuse stratification due to variations in concentrations of basalt lapilli and/or pebbles and cobbles. These massive beds are inferred to have been deposited by concentrated granular flows composed of ash rapidly remobilized during or shortly after surge deposition, along with entrained pre-eruptive surface rubble; their presence indicates that pyroclastic surge material was deposited upstream in steep drainage headwaters. The lack of interbedded laminated or cross-laminated ash might mean that the parent surges did not reach the

Table 1
Described Study Site Locations and Characteristics

Site	Latitude (degrees)	Longitude (degrees)	Distance (direction) from crater center (m)	Total thickness[a] (m)	Setting	Facies present[b]	Notes
U20-38	37.0198	−117.4478	1120 (N)	0.98	Top of gently sloping (toward crater) mesa.	LXL	Eroded top
U20-55	37.0359	−117.4605	3000 (NNW)	0.10	Flat valley floor.	LXL	Capped by 4 cm reworked
U20-62	36.9745	−117.4603	4040 (SSW)	1.2	~50 m wide, gently sloping channel below confluences with at least three steep mountainside channels.	MLT	Capped by likely debris flow deposit, 0.8 m thick
U21-26	37.0259	−117.4638	2115 (NW)	0.36	Flat valley floor.	LXL	Weathered top, no apparent erosion
U21-27	37.0233	−117.4627	1810 (NW)	0.48	Flat valley floor.	LXL	Weathered top, upper few cm A_v, no apparent erosion
U22-3	37.0815	−117.4942	8960 (NNW)	0.05	~2 m-high side of channel cut into pre-Ubehebe playa deposits.	LXL	Isolated distal remnant of Ubehebe Crater deposits, overlain by fluvial deposits
U22-7	37.0293	−117.4932	4280 (NW)	~0.03	Alluvial fan sourced from mountains west of Ubehebe	LXL	Deposit disrupted by bioturbation
U22-11	36.9984	−117.4731	7130 (SSW)	0.45	Upper fan near mouth of small canyon	MLT	Ubehebe Crater deposit underlain and overlain by loose angular cobbles
U22-16	37.0103	−117.4179	2880 (E)	0.41	Bank of channel on edge of alluvia fan fed from Tin Mtn	MLT	Erosive upper contact with overlying fluvial sand and gravel
U22-19	36.9970	−117.8485	2760 (SE)	~1	Alluvial fan fed from Tin Mtn	MLT	Eroded/weathered top littered with cobbles
UB-6-1	37.0454	−117.4209	4770 (NE)	0.01	Alluvial fan fed from mountains to NE of Ubehebe Crater	LXL	Orange-tan very fine to fine ash; well-defined layer in sharp contact with alluvial fan deposit above and intact S-fall below
Sec-59	37.0570	−117.4310	5540 (NNE)	0.01	Channel draining mountains to NE of Ubehebe Crater	LXL	Orange-tan very fine ash in sharp contact with fluvial deposits above and intact S-fall below

Table 1
Continued

Site	Latitude (degrees)	Longitude (degrees)	Distance (direction) from crater center (m)	Total thickness[a] (m)	Setting	Facies present[b]	Notes
Sec-60	37.0869	−117.4823	8960 (NNW)	0.001–0.003	Alluvial fan fed from mountains to NE of Ubehebe Crater	LXL	Pale orange very fine ash overlain by fluvial deposits; rests on intact S-fall
Sec-63	37.0777	−117.4727	7770 (N)	0.01	Channel draining mountains to NE of Ubehebe Crater	LXL	Pale orange very fine ash overlain by aeolian sand; in sharp contact with S-fall below

[a]Total thickness of undisturbed deposits from Ubehebe Crater only, not including potential underlying deposits from preceding phases of activity or reworked deposits that might overlie undisturbed material. [b]LXL—laminated and cross laminated ash; MLT—massive lapilli tuff.

observation sites, while the granular flows did. More likely, such stratified ash horizons were eroded and incorporated during propagation of the granular flows, as has been documented elsewhere around Ubehebe Crater (Valentine et al., 2022).

4. Comparison With Other Maar Deposits—Is Ubehebe Crater Unusual?

Sandri et al. (2012) compiled runout distances for 26 maar-forming eruptions; these are primarily based upon lateral extents of surge deposits in the geologic record. Most of these distances are in the range of 1–4 km, with some "large" examples ranging between 5 and 6 km. Note that they listed the Ubehebe Crater surge runout as 0.82 km, which is based upon Wohletz and Sheridan (1979), who studied less than 10% of the lateral extent of the deposits in only one sector. Examples published since, or not included in, Sandri et al.'s (2012) compilation include: Karymskoye lake 1996 (1.3 km; eruption observations of Belousov & Belousova, 2001), Maungatake-take maar (2.25 km based upon model estimates; Brand et al., 2014), Parrumbete (~2.5 km from crater center, Jordan et al., 2013), Table Rock (Oregon, >5 km; Brand & Clarke, 2012), Haskie (Hopi Buttes, Arizona, 1.2 km; Vazquez & Ort, 2006), and Kilbourne Hole (New Mexico, ~8 km from crater center; Vitarelli, 2020); unless otherwise noted, these are all based on preserved deposits. The 5-cm thickness of Ubehebe Crater pyroclastic surge deposits at ~9 km suggests that the parent surges are likely to have extended farther, perhaps by 1–3 km based on thinning rate, although it is possible that the 9 km site is near a location of buoyancy reversal/liftoff of the farthest-reaching surges, which may have resulted in enhanced sedimentation (Andrews & Manga, 2012).

Was the Ubehebe Crater eruptive activity unusual? The crater dimensions are typical compared to maar craters around the world (Graettinger, 2018), suggesting that Ubehebe Crater did not involve unusually large volume, or unusually energetic, explosions (although caution must be used in equating crater size to explosion energy when multiple explosions are involved; Sonder et al., 2015). There is relatively little relief between the crater and the most distal preserved deposit (U22-3; Figure 1a) so that there would have been little or no assistance to flow by a slope; in fact, the most distal site is approximately the same altitude as the crater rim.

We conclude that Ubehebe Crater deposits are preserved at larger distances compared to other documented cases because they are young (~2100 years) and because of the arid setting of Death Valley. Here there is little bioturbation, limited erosion in low-relief areas, and soil-forming processes are very gradual. Note that this is a similar situation to that at Kilbourne Hole (~20 ka) in the desert of southern New Mexico, with its surge deposits extending to ~8 km from crater center (Vitarelli, 2020). Moore (1967) documented sandblasting of vegetation at distances of ~6 km from vent during the 1965 eruption of Taal volcano, and total runout must have extended beyond this. To summarize, we think that the pyroclastic surge runout associated with Ubehebe Crater may be typical of phreatomagmatic maar-forming eruptions, but that in most cases the runout is underestimated due to poor preservation of distal deposits.

5. Low Temperatures Contribute to Long Phreatomagmatic Pyroclastic Surge Runouts

Runout of >9 km intuitively seems far for such a small-volume deposit, especially when one considers that the total volume is the result of multiple, much smaller-volume, pyroclastic surges related to individual explosions. We hypothesize that relatively low temperatures promoted the long runout of these dilute pyroclastic currents. Pyroclastic surges sourced from phreatomagmatic explosions are likely to have relatively low temperatures compared to other explosive volcanic phenomena because: (a) much initial magma heat is used up in fueling fragmentation and vapourizing groundwater; (b) the ejecta is typically rich in country rock-derived lithic clasts from fine ash to block size. Ubehebe Crater surge deposits typically contain 10–50 vol.% lithic material, as measured in the 1 mm size fraction, and much of the basaltic material in the remaining fraction is likely to have been recycled and thus not a major contributor to surge temperatures. Many phreatomagmatic pyroclastic surges may have temperatures of ~100–300°C as they begin to propagate outward. For example, plastering of damp ash onto surfaces at Taal and Capelinhos during historical eruptions further indicates sub-boiling temperatures (Waters & Fisher, 1971), although we see no evidence that the Ubehebe Crater surges were wet (Valentine et al., 2021).

A surge's mixture density (particles plus gas) must be larger than the ambient air density (~1.1 kg/m^3 at the altitude of Ubehebe Crater) in order for it to propagate. As a surge propagates outward, it loses particles to sedimentation, and mixing with air along the top and lateral margins dilutes the mixture. Both of these processes reduce the mixture density during propagation (e.g., Andrews & Manga, 2012; Valentine et al., 2011). If a pyroclastic surge has a high temperature, entrained air is heated and expands, adding to the dilution effect; additionally, buoyant plumes may form along the top of the current, which rise and draw air inward, exerting additional drag on the front of the surge and slowing it down while also robbing material from the lateral current. A low-temperature surge will also be diluted due to entrainment, but with less of an effect from air heating/expansion and weaker, if any, buoyant plumes rising from its top. Thus, low temperatures act in favor of longer runout; similar effects have been experimentally demonstrated for hot and cold subaqueous flows (turbidity currents; Cantelli et al., 2008).

We illustrate these effects with two numerical simulations of pyroclastic surges with different initial temperatures (Figure 2). Both simulations solve conservation of mass, momentum, and energy for gas and particle phases as overlapping continua that interact via drag and heat transfer (nomenclature in Table 2; Benyahia et al., 2012):

$$\frac{\partial}{\partial t}\left(\epsilon_g \rho_g\right) + \frac{\partial}{\partial x_j}\left(\epsilon_g \rho_g U_{gj}\right) = 0 \quad \text{(gas)}, \tag{1}$$

$$\frac{\partial}{\partial t}\left(\epsilon_m \rho_m\right) + \frac{\partial}{\partial x_j}\left(\epsilon_m \rho_m U_{mj}\right) = 0 \quad \text{(particles)}, \tag{2}$$

$$\frac{\partial}{\partial t}\left(\epsilon_g \rho_g U_{gi}\right) + \frac{\partial}{\partial x_j}\left(\epsilon_g \rho_g U_{gj} U_{gi}\right) = -\epsilon_g \frac{\partial P_g}{\partial x_i} + \frac{\partial \tau_{gij}}{\partial x_j} - \sum_{m=1}^{M} I_{gmi} + \epsilon_g \rho_g g_i \quad \text{(gas)}, \tag{3}$$

$$\frac{\partial}{\partial t}\left(\epsilon_m \rho_m U_{mi}\right) + \frac{\partial}{\partial x_j}\left(\epsilon_m \rho_m U_{mj} U_{mi}\right) = -\epsilon_m \frac{\partial P_g}{\partial x_i} + \frac{\partial \tau_{mij}}{\partial x_j} + I_{gmi} - \sum_{l=1}^{M} I_{mli} + \epsilon_m \rho_m g_i \quad \text{(particles)} \tag{4}$$

$$\epsilon_g \rho_g C_{pg}\left[\frac{\partial T_g}{\partial t} + U_{gj}\frac{\partial T_g}{\partial x_j}\right] = -\frac{\partial q_{gj}}{\partial x_j} + \sum_{m=1}^{M} \gamma_{gm}\left(T_m - T_g\right) + \gamma_{Rg}\left(T_{Rg}^4 - T_g^4\right) \quad \text{(gas)} \tag{5}$$

and

$$\epsilon_m \rho_m C_{pm}\left[\frac{\partial T_m}{\partial t} + U_{mj}\frac{\partial T_m}{\partial x_j}\right] = -\frac{\partial q_{mj}}{\partial x_j} - \gamma_{gm}\left(T_m - T_g\right) + \gamma_{Rm}\left(T_{Rm}^4 - T_m^4\right) \quad \text{(particles)}. \tag{6}$$

The solids stress tensor τ_{mij} in Equation 4 is

$$\tau_{mij} = \tau_{mij}^k + \tau_{mij}^f \tag{7}$$

where the k and f superscripts refer to the kinetic and frictional components of stress. The solids stresses are modeled with an additional conservation equation for granular temperature ($\Theta_m = \frac{1}{3}\left\langle u_{mi}'^{\,2}\right\rangle$, where u_{mi}' is the

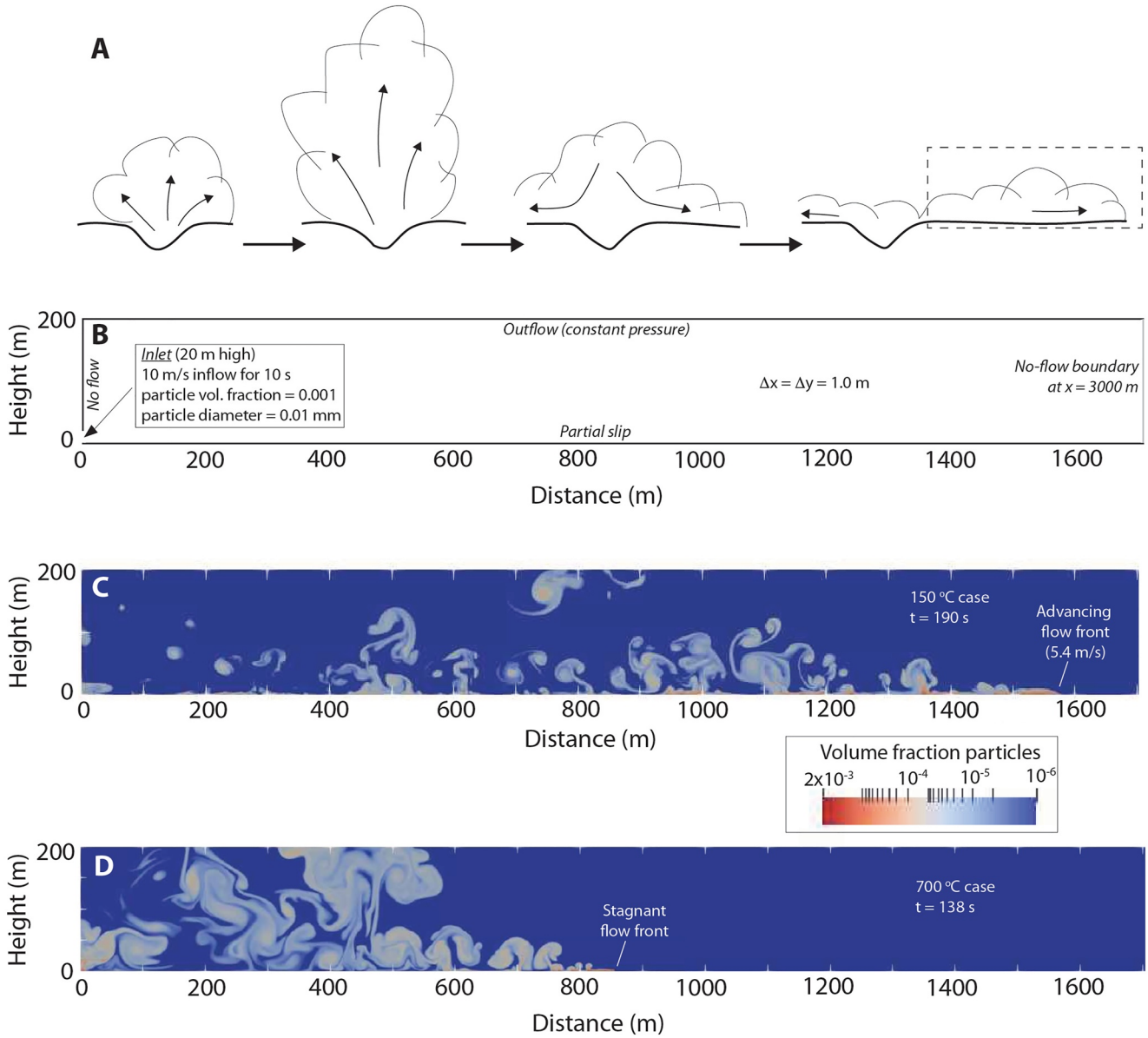

Figure 2. Two simplified numerical experiments illustrating the effect of temperature on pyroclastic surge runout. (a) Conceptual illustration progression of a phreatomagmatic explosion jet rising and then collapsing to feed laterally flowing pyroclastic surges. Dashed rectangle in final frame represents the computational domain described below. (b) Boundary conditions and grid resolution are indicated; the latter is intended to resolve most scales of turbulence that govern large-scale entrainment processes. The no-flow boundary at right-hand side is far from the dynamics of interest in order to minimize boundary effects. A gas (air)-particle mixture is injected via the inlet at base of left boundary. (c) Low temperature (150°C) case. At 190 s after beginning of mixture inflow, the advancing density current has reached ~1,580 m, and has a flow front speed of 5.4 m/s (flow front temperature 97°C). (d) High temperature (700°C) case. Flow front advance has stalled only 138 s after initiation of inflow at a distance of 850 m (flow front temperature 346°C). Note well developed buoyant plume rising from surface of the current.

fluctuating velocity component of particle class m in the ith direction and the angle brackets indicate ensemble average):

$$\frac{2}{3}\rho_m\left[\frac{\partial \epsilon_m \Theta_m}{\partial t}+\frac{\partial \epsilon_m U_{mj}\Theta_m}{\partial x_j}\right]=\frac{\partial}{\partial x_i}\left(\kappa_m\frac{\partial \Theta_m}{\partial x_i}\right)+\tau^k_{mij}\frac{\partial U_{mi}}{\partial x_j}+\Pi_m-\epsilon_m\rho_m J_m. \quad (8)$$

The first term on the right-hand side of Equation 8 is conduction of granular temperature, the second is production through shear, the third is dissipation due to particle-fluid drag, and the final term is dissipation through inelastic collisions (Benyahia et al., 2012). Closure equations for the right-hand side terms of Equation 8 are

Table 2
Notation

Symbol	Definition; units
C_{DM}	Multiparticle drag coefficient; J/kg·K
C_{pg}	Specific heat of the gas; J/kg·K
C_{pm}	Specific heat of the mth phase; J/kg·K
g_i	Acceleration due to gravity; m/s^2
i, j, k	Subscripts for identifying vector and tensor components; if there are multiple subscripts, these indices appear at the end of the list of subscripts and summation convention is implied only for these indices
I_{mli}	Momentum transfer between the mth and the lth phases due to interphase drag force; N/m^3
J_m	Collisional dissipation of granular temperature of mth phase; m^2/s^3
M	Total number of solid phases
P_g	Gas-phase pressure; Pa
q_{gj}	Conductive heat flux in the gas; J/m^2·s
q_{mj}	Conductive heat flux in the mth phase; J/m^2·s
t	Time; s
T_g	Thermodynamic temperature of the gas; K
T_m	Thermodynamic temperature of the mth phase; K
T_{Rm}	Background temperature in a radiation model; K
U_{mj}	Jth component of the mth phase velocity; m/s
U_{gj}	Jth component of the gas velocity; m/s
x_j	Jth coordinate direction; m
γ_{gm}	Gas-solid heat transfer coefficient; J/m^3·K·s
γ_{Rm}	Radiative heat transfer coefficient for the mth phase; J/m^3·K^4·s
ϵ_g	Volume fraction of gas
ϵ_m	Volume fraction of the mth phase
κ_m	Conductivity of granular temperature; kg/m·s
Π_m	Dissipation of granular temperature via gas-particle drag; kg/m·s^3
Θ_m	Granular temperature of the mth phase; m^2/s^2
ρ_m	Material density of the mth phase; kg/m^3
ρ_g	Density of the gas phase; kg/m^3
τ_{gij}	Stress tensor of the gas; Pa
τ_{mij}	Stress tensor of the mth phase; Pa
τ^f_{mij}	Frictional component of the stress tensor of the mth phase; Pa
τ^k_{mij}	Kinetic component of the stress tensor of the mth phase; Pa

derived from the kinetic theory approach of Srivastava and Sundaresan (2003), and are summarized in Breard et al. (2019) and Valentine (2020), as are constitutive models for the other governing equations. The governing conservation equations are solved with the open-source, finite-volume code MFIX v. 2016.1 (see Data Availability Statement); initial and boundary conditions and material properties are described in the Table 3. Rather than applying a turbulence model, which remains an active area of research for multiphase flows (e.g., Beetham et al., 2021; Saeedipour & Schneiderbauer, 2022), the simulations are intended to have sufficient resolution (1 m) to directly model most eddies that contribute significantly to entrainment, sufficient for this qualitative comparison of cool and hot flows.

Surges are simulated by introducing a gas-particle mixture into a domain filled with air via an inlet at the lower left-hand boundary, with a speed of 10 m/s for a duration of 10 s, mimicking the short duration of a collapsing

Table 3
Initial and Boundary Conditions, and Material Properties

Domain size	200 m high, 3,000 m wide
Coordinate system	Cartesian, two-dimensions
Boundary conditions	
• Left side above inlet	• No flow
• Top	• Outflow (constant pressure)
• Inlet	• Mass inflow (see below)
• Right side	• No flow
• Bottom	• Partial slip wall
Inlet condition (mass inflow)	
• Inlet height (bottom of left boundary)	• 20 m
• Gas type	• Air
• Gas pressure	• 10^5 Pa
• Inflow temperature	• 150, 700°C (Figures 2c and 2d, respectively)
• Particle volumetric concentration	• 10^{-3} (150°C case), 1.23×10^{-3} (700°C case)
• Inflow speed (horizontal)	• 10 m/s
• Inflow granular temperature	• 0.01 m^2/s^2
• Inflow duration	• 10 s
Computational grid	Uniform, $\Delta x = \Delta y = 1$ m, 6×10^5 cells
Initial conditions	
• Gas type	• Air
• Gas pressure	• 10^5 Pa
• Temperature	• 20°C
• Gas properties (air)	• Burcat and Ruscic (2005) thermochemical database
Particle properties	
• Density	• 2,000 kg m^{-3}
• Heat capacity	• 954 J kg^{-1} K^{-1}
• Diameter	• 0.01 mm
• Coefficient of restitution	• 0.5
• Coefficient of friction	• 0.5
• Angle of internal friction	• 28°
• Maximum packing volume fraction	• 0.64

phreatomagmatic explosion jet (Figures 2a and 2b). The two cases (low and high temperature) have the same initial ratio of potential and kinetic energies, as expressed by the Richardson number (Bursik & Woods, 1996):

$$Ri = \frac{(\rho_{mix} - \rho_{air})\, g h}{\rho_{mix} U^2} \tag{9}$$

where ρ_{mix} is the density of the inflowing mixture, ρ_{air} is the ambient air density, g is gravitational acceleration, h is the inlet height, and U is the horizontal speed at the inlet. This means that the particle concentration the higher-temperature simulation is slightly larger than that of the low-temperature case, in order to compensate for the lower gas density of the former (Table 3). The front of a low-temperature (150°C) simulated surge reaches a distance of 1580 m at 190 s after initiation and it is still advancing at a speed of 5.4 m/s (Figure 2c). In contrast, the high-temperature (700°C) current ceases propagation at a distance of 850 m and time of 138 s; this is due to the entrainment and heating of air and the formation of buoyant plumes that rise from the surge, depleting it of material and causing inward directed wind that acts against flow advance (Figure 2d). These two simulations are not intended to directly simulate an individual surge out of the many that occurred at Ubehebe Crater, but rather to

illustrate how low temperatures of pyroclastic surges from phreatomagmatic explosions can promote long runout. The effects of high temperature on reducing surge runout are even more pronounced in three dimensions, where entrainment and development of buoyancy along the sides of a current (not just its top) can also greatly reduce a current's ability to spread radially (Andrews, 2014).

6. Implications for Hazard Assessment in Volcanic Fields

Pyroclastic surges can have devastating effects on people and infrastructure, even at speeds of a few meters per second (Jenkins et al., 2013; Valentine, 1998). At temperatures as low as 100°C (Baxter et al., 2017), the fine ash load of a surge can cause severe burns and asphyxiation for humans and animals as well as harm to infrastructure such as air intakes and internal combustion engines. Thus, realistic estimates of the distances that could be reached by future phreatomagmatic, low-temperature pyroclastic surges are important for hazard assessments and emergency planning in areas that might be subjected to such volcanic activity. We suspect that previous hazard assessments, which relied on runout distances based on deposits preserved around maar volcanoes, might have underestimated their potential hazard footprint. We recommend that future assessments consider potential surge runout distances of 10–15 km from their source maar volcanoes.

Data Availability Statement

All data for this study are presented in this paper. The code use for all simulations is the two-fluid model in MFIX v. 2016.1 and is publicly available at https://mfix.netl.doe.gov.

Acknowledgments
Numerical simulations were conducted at the University at Buffalo's Center for Computational Research. The work was funded by NSF Grant EAR-2035260 to Valentine, the U.S. Geological Survey, and by support from DEVORA (Determining Volcanic Risk for Auckland) to White. Field research was conducted with permission of Death Valley National Park. Any use of trade, firm, or product names is for descriptive purposes only and does not imply endorsement by the U.S. Government.

References

Andrews, B. J. (2014). Dispersal and air entrainment in unconfined dilute pyroclastic density currents. *Bulletin of Volcanology*, *76*(9), 852. https://doi.org/10.1007/s00445-014-0852-4

Andrews, B. J., & Manga, M. (2012). Experimental study of turbulence, sedimentation, and coignimbrite mass partitioning in dilute pyroclastic density currents. *Journal of Volcanology and Geothermal Research*, *225–226*, 30–44. https://doi.org/10.1016/j.jvolgeores.2012.02.011

Baxter, P. J., Jenkins, S., Seswandhana, R., Komorowski, J.-C., Dunn, K., Purser, D., et al. (2017). Human survival in volcanic eruptions: Thermal injuries in pyroclastic surges, their causes, prognosis, and emergency management. *Burns*, *43*(5), 1051–1069. https://doi.org/10.1016/j.burns.2017.01.025

Beetham, S., Fox, R. O., & Capecelatro, J. (2021). Sparse identification of multiphase turbulence closures for coupled fluid-particle flows. *Journal of Fluid Mechanics*, *914*, A11. https://doi.org/10.1017/jfm.2021.53

Belousov, A., & Belousova, M. (2001). *Eruptive processes, effects and deposits of the 1996 and the ancient basaltic phreatomagmatic eruptions in Karymskoye lake, Kamchatka, Russia* (Vol. 30, pp. 35–60). Special Publications of the International Association of Sedimentologists.

Benyahia, S., Syamlal, M., & O'Brien, T. J. (2012). Summary of MFIX equations. Retrieved from https://mfix.netl.doe.gov/doc/mfix-archive/mfix_current_documentation/MFIXEquations2012-1.pdf

Brand, B. D., & Clarke, A. B. (2012). An unusually energetic basaltic phreatomagmatic eruption: Using deposit characteristics to constrain dilute pyroclastic density current dynamics. *Journal of Volcanology and Geothermal Research*, *243–244*, 81–90. https://doi.org/10.1016/j.jvolgeores.2012.06.011

Brand, B. D., Gravley, D. M., Clarke, A. B., Lindsay, J. M., Bloomberg, S. H., Augustin-Flores, J., & Németh, K. (2014). A combined field and numerical approach to understanding dilute pyroclastic density current dynamics and hazard potential: Auckland Volcanic Field, New Zealand. *Journal of Volcanology and Geothermal Research*, *276*, 215–232. https://doi.org/10.1016/j.jvolgeores.2014.01.008

Breard, E. C. P., Dufek, J., & Roche, O. (2019). Continuum modeling of pressure-balanced and fluidized granular flows in 2-D: Comparison with glass bead experiments and implications for concentrated pyroclastic density currents. *Journal of Geophysical Research: Solid Earth*, *124*(6), 5557–5583. https://doi.org/10.1029/2018JB016874

Burcat, A., & Ruscic, B. (2005). *Third Millennium ideal gas and condensed phase thermochemical database for combustion with updates from active thermochemical tables (Rep. ANL-05/20 TAE 960)*. Argonne National Laboratory.

Bursik, M. I., Kurbatov, A. V., Sheridan, M. F., & Woods, A. W. (1998). Transport and deposition in the May 18, 1980, Mount St. Helens blast flow. *Geology*, *26*(2), 155–158. https://doi.org/10.1130/0091-7613(1998)026<0155:taditm>2.3.co;2

Bursik, M. I., & Woods, A. W. (1996). The dynamics and thermodynamics of large ash flows. *Bulletin of Volcanology*, *58*(2–3), 175–193. https://doi.org/10.1007/s004450050134

Cantelli, A., Johnson, S., White, J. D. L., & Parker, G. (2008). Sediment sorting in the deposits of turbidity currents created by experimental modeling of explosive subaqueous eruptions. *The Journal of Geology*, *116*(1), 76–93. https://doi.org/10.1086/524676

Champion, D. E., Cyr, A., Fierstein, J., & Hildreth, W. (2018). Monogenetic origin of Ubehebe Crater maar volcano, Death Valley, California: Paleomagnetic and stratigraphic evidence. *Journal of Volcanology and Geothermal Research*, *354*, 67–73. https://doi.org/10.1016/j.jvolgeores.2017.12.018

Crowe, B. M., & Fisher, R. V. (1973). Sedimentary structures in base-surge deposits with special reference to cross-bedding, Ubehebe Craters, Death Valley, California. *The Geological Society of America Bulletin*, *84*(2), 663–682. https://doi.org/10.1130/0016-7606(1973)84<663:ssibdw>2.0.co;2

Fierstein, J., & Hildreth, W. (2017). Eruptive history of the Ubehebe Crater cluster, Death Valley, California. *Journal of Volcanology and Geothermal Research*, *335*, 128–146. https://doi.org/10.1016/j.jvolgeores.2017.02.010

Graettinger, A. H. (2018). Trends in maar crater size and shape using the global Maar Volcano Location and Shape (MaarVLS) database. *Journal of Volcanology and Geothermal Research*, *357*, 1–13. https://doi.org/10.1016/j.jvolgeores.2018.04.002

Jenkins, W., Komorowski, J.-C., Baxter, P. J., Spence, R., Picquout, A., Lavigne, F., & Surono (2013). The Merapi 2010 eruption: An interdisciplinary impact assessment methodology for studying pyroclastic density current dynamics. *Journal of Volcanology and Geothermal Research*, *261*, 316–329. https://doi.org/10.1016/j.jvolgeores.2013.02.012

Jordan, S. C., Cas, R. A. F., & Hayman, P. C. (2013). The origin of a large (>3 km) maar volcano by coalescence of multiple shallow craters: Lake Parrumbete maar, southeastern Australia. *Journal of Volcanology and Geothermal Research*, *254*, 5–22. https://doi.org/10.1016/j.jvolgeores.2012.12.2019

Moore, J. G. (1967). Base surge in recent volcanic eruptions. *Bulletin Vulcanologique*, *30*(1), 337–363. https://doi.org/10.1007/bf02597678

Saeedipour, M., & Schneiderbauer, S. (2022). Toward a universal description of multiphase turbulence phenomena based on the vorticity transport equation. *Physics of Fluids*, *34*(7), 073317. https://doi.org/10.1063/5.0098824

Sandri, L., Jolly, G., Lindsay, J., Howe, T., & Marzocchi, W. (2012). Combining long- and short-term probabilistic volcanic hazard assessment with cost-benefit analysis to support decision making in a volcanic crisis from the Auckland Volcanic Field, New Zealand. *Bulletin of Volcanology*, *74*(3), 705–723. https://doi.org/10.1007/s00445-011-0556-y

Sonder, I., Graettinger, A. H., & Valentine, G. A. (2015). Scaling multiblast craters: General approach and application to volcanic craters. *Journal of Geophysical Research: Solid Earth*, *120*(9), 6141–6158. https://doi.org/10.1002/2015JB012018

Srivastava, A., & Sundaresan, S. (2003). Analysis of a frictional-kinetic model for gas-particle flow. *Powder Technology*, *129*(1–3), 72–85. https://doi.org/10.1016/s0032-5910(02)00132-8

Valentine, G. A. (1998). Damage to structures by pyroclastic flows and surges, inferred from nuclear weapons effects. *Journal of Volcanology and Geothermal Research*, *87*(1–4), 117–140. https://doi.org/10.1016/s0377-0273(98)00094-8

Valentine, G. A. (2020). Initiation of dilute and concentrated pyroclastic currents from collapsing mixtures and origin of their proximal deposits. *Bulletin of Volcanology*, *82*(2), 20. https://doi.org/10.1007/s00445-020-1366-x

Valentine, G. A., & Connor, C. B. (2015). Basaltic volcanic fields. In H. Sigurdsson, B. Houghton, S. R. McNutt, H. Rymer, & J. Stix (Eds.), *The encyclopedia of volcanoes* (2nd ed., pp. 423–439). Elsevier. https://doi.org/10.1016/B978-0-12-385938-9.00023-7

Valentine, G. A., Doronzo, D. M., Dellino, P., & de Tullio, M. D. (2011). Effects of volcano profile on dilute pyroclastic density currents: Numerical simulations. *Geology*, *39*(10), 957–950. https://doi.org/10.1130/G31936.1

Valentine, G. A., Fierstein, J., & White, J. D. L. (2021). Soft sediment deformation in dry pyroclastic deposits at Ubehebe Crater, Death Valley, California. *Geology*, *49*(2), 211–215. https://doi.org/10.1130/G48147.1

Valentine, G. A., Fierstein, J., & White, J. D. L. (2022). Pyroclastic deposits of Ubehebe Crater (Death Valley, California): Ballistics, pyroclastic surges, and dry granular flows. *Geosphere*. https://doi.org/10.1130/GES02526.1

Valentine, G. A., & White, J. D. L. (2012). Revised conceptual model for maar-diatremes: Subsurface processes, energetics, and eruptive processes. *Geology*, *40*(12), 1111–1114. https://doi.org/10.1130/G33411.1

Vazquez, J. A., & Ort, M. H. (2006). Facies variation of eruption units produced by the passage of single pyroclastic surge currents, Hopi Buttes volcanic field, USA. *Journal of Volcanology and Geothermal Research*, *154*(3–4), 222–236. https://doi.org/10.1016/j.jvolgeores.2006.01.003

Vitarelli, D. C. (2020). *Eruptive volume and explosion energy estimates from Kilbourne Hole maar, south-central New Mexico*, (Masters thesis) (p. 139). Las Cruces, New Mexico State University.

Waters, A. C., & Fisher, R. V. (1971). Base surges and their deposits: Capelhinos and Taal volcanoes. *Journal of Geophysical Research*, *76*(23), 5596–5614. https://doi.org/10.1029/jb076i023p05596

White, J. D. L., & Houghton, B. F. (2006). Primary volcaniclastic rocks. *Geology*, *34*(8), 677–680. https://doi.org/10.1130/G22346.1

White, J. D. L., & Ross, P.-S. (2011). Maar-diatreme volcanoes: A review. *Journal of Volcanology and Geothermal Research*, *201*(1–4), 1–29. https://doi.org/10.1016/j.volgeores.2011.01.010

Wild, A. J., Bebbington, M. S., Lindsay, J. M., & Charlton, D. H. (2021). Modelling spatial population exposure and evacuation clearance time for the Auckland Volcanic Field, New Zealand. *Journal of Volcanology and Geothermal Research*, *416*, 107282. https://doi.org/10.1016/j.jvolgeores.2021.107282

Wohletz, K. H., & Sheridan, M. F. (1979). *A model of pyroclastic surge* (Vol. 180, pp. 177–194). Geological Society of America Special Paper.